Molecular-Level Design of Pyrrhotite Electrocatalyst Decorated Hierarchical Porous Carbon Spheres as Nanoreactors for Lithium–Sulfur Batteries

Yash Boyjoo, Haodong Shi, Emilia Olsson, Qiong Cai, Zhong-Shuai Wu, Jian Liu,* and Gao Qing (Max) Lu*

Lithium–sulfur batteries (LSBs) are a class of new-generation rechargeable high-energy-density batteries. However, the persisting issue of lithium polysulfides (LiPs) dissolution and the shuttling effect that impedes the efficiency of LSBs are challenging to resolve. Herein a general synthesis of highly dispersed pyrrhotite Fe$_{1-x}$S nanoparticles embedded in hierarchically porous nitrogen-doped carbon spheres (Fe$_{1-x}$S-NC) is proposed. Fe$_{1-x}$S-NC has a high specific surface area (627 m^2 g^{-1}), large pore volume (0.41 cm^3 g^{-1}), and enhanced adsorption and electrocatalytic transition toward LiPs. Furthermore, in situ generated large mesoporous pores within carbon spheres can accommodate high sulfur loading of up to 75%, and sustain volume variations during charge/discharge cycles as well as improve ionic/mass transfer. The exceptional adsorption properties of Fe$_{1-x}$S-NC for LiPs are predicted theoretically and confirmed experimentally. Subsequently, the electrocatalytic activity of Fe$_{1-x}$S-NC is thoroughly verified. The results confirm Fe$_{1-x}$S-NC is a highly efficient nanoreactor for sulfur loading. Consequently, the Fe$_{1-x}$S-NC nanoreactor performs extremely well as a cathodic material for LSBs, exhibiting a high initial capacity of 1070 mAh g^{-1} with nearly no capacity loss after 200 cycles at 0.5 C. Furthermore, the resulting LSBs display remarkably enhanced rate capability and cyclability even at a high sulfur loading of 8.14 mg cm^{-2}.

1. Introduction

Lithium–sulfur batteries (LSBs) are a new generation of rechargeable batteries with a superior theoretical specific energy of 2600 Wh kg^{-1} and are recognized as one of high energy density storage devices for practical applications. In LSBs the cathode material is mainly sulfur, which is abundantly available, low cost, environmentally friendly and has high theoretical capacity of 1675 mAh g^{-1}.[1–6] However, the challenging issues associated with sulfur-based cathodes are: 1) the low electrical conductivity of sulfur, 2) the dissolution and shuttling effects of lithium polysulfides (LiPs), and 3) large volume variations during charge/discharge cycles. These bring about low efficiency, poor cycling stability, self-discharge phenomena, and ultimately degradation of the electrode material, all of which currently limit the potential commercialization of LSBs. These drawbacks, especially the difficulty to confine LiPs are the current research priorities in the field of LSBs.[1,7,8]

To overcome these problems, a vast amount of research has been carried out in the last decade. The encapsulation of sulfur in a conductive carbon host can effectively improve the electrical conductivity of sulfur. Moreover, carbon offers a physical barrier that encapsulates the LiP intermediates.[9–12] Nevertheless, such weak physical confinement is not enough to suppress the eventual diffusion of LiPs over time.[13] Due to the polar nature of LiPs, the strategies involving functional polar substrates as

---

Dr. Y. Boyjoo, Prof. J. Liu
State Key Laboratory of Catalysis
Dalian Institute of Chemical Physics
Chinese Academy of Sciences
457 Zhongshan Road, Dalian 116023, China
E-mail: jian.liu@surrey.ac.uk

The ORCID identification number(s) for the author(s) of this article can be found under https://doi.org/10.1002/aenm.202000651.

© 2020 The Authors. Published by WILEY-VCH Verlag GmbH & Co. KGaA, Weinheim. This is an open access article under the terms of the Creative Commons Attribution License, which permits use, distribution and reproduction in any medium, provided the original work is properly cited.

DOI: 10.1002/aenm.202000651

H. D. Shi, Prof. Z.-S. Wu
Dalian National Laboratory for Clean Energy
Dalian Institute of Chemical Physics
Chinese Academy of Sciences
457 Zhongshan Road, Dalian 116023, China
E-mail: wuzs@dicp.ac.cn

H. D. Shi
University of Chinese Academy of Sciences
19 A Yuquan Rd, Shijingshan District, Beijing 100049, China

Dr. E. Olsson, Prof. Q. Cai, Prof. J. Liu, Prof. G. Q. Lu
DICP-Surrey Joint Centre for Future Materials
Department of Chemical and Process Engineering
and Advanced Technology Institute
University of Surrey
GU2 7XH, Guildford, UK

efficient sulfur hosts have been employed for LSBs. N-doped carbons could solve this problem to a certain degree. However the trapped LiPs could not be recycled,[14] which ultimately reduce the utilization efficiency of sulfur. Host materials such as transition metal oxides, carbides, nitrides, and sulfides have been thoroughly investigated and their strong chemical bonding with LiPs can indeed provide an effective solution to promote the diffusion and catalytic conversion of soluble LiPs.[15–22] However, high mass density and inherent low surface area of these materials limit their sulfur loading (<56 wt%).[13] Finally, to address the issue of volumetric variations during charge/discharge cycles, a variety of nanoarchitectures that contain voids or empty space such as mesoporous spheres, hollow structures, yolk–shell particles and multishells have been developed as nanoreactors.[23–30] However, such designs require complicated synthetic steps and the use of sacrificial templates to endow an empty space within those materials. On accounts of those inadequacies, it becomes obvious that ideal sulfur host materials should possess: 1) high electrical conductivity, 2) low density that provides both physical and chemical confinement to LiPs, 3) dispersed catalysts that can strongly adsorb and electrocatalytically reduce LiPs, and 4) hierarchical pores such as micropores, mesopores and large voids/cavities to accommodate a high sulfur loading, buffer the volume change during charge/discharge cycles as well as improve the mass transfer of electrolyte to/from active sites, are greatly desired. Furthermore, the synthesis process should be straightforward and avoid the use of sacrificial templates.

Metal sulfides such as Co_9S_8, CoS_2, FeS, FeS_2, TiS_2, MnS, SnS_2, VS_2, and WS_2[15,16,31–34] have been developed as cathode material for LSBs, due to their strong abilities for LiPs adsorption followed by their subsequent electrocatalytic redox reaction, which improves sulfur utilization.[15] However, metal sulfides generally have poor electrical conductivity and high gravimetric density. To address these issues, recently nanostructural metal sulfides combined with carbon materials such as ultrathin TiS_2 nanosheets layered with N, S codoped carbon,[35] interlaced carbon nanotubes threaded hollow Co_3S_4 nanoboxes,[36] polypyrrole on CoS nanoboxes,[37] and CoS_2 nanoparticles embedded in porous carbon[38] have been reported.

Fe and S are commonly occurring elements on earth. It would therefore be a cheap and sustainable alternative to use iron sulfide based compounds as electroactive catalysts in LSBs. Compared to other metal sulfides, hexagonal pyrrhotite ($Fe_{1-x}S$) has an uncharacteristically high metallic type conductivity.[39] It was also found that FeS_2 (pyrite) could substantially reduce the out-diffusion of dissolved LiPs from sulfur cathodes and consequently improve the cycling performance of LSBs.[40] In addition, the FeS phase demonstrated inferior cycling stability in LSBs compared to other transition metal sulfides (only 47.4% capacity retention after 300 cycles).[34] Therefore the choice of the phase type of iron sulfide compound is of utmost importance for the design of a high-performance LSB cathode. Consequently, it is considered that $Fe_{1-x}S$ should be an ideal electrocatalyst for LSBs due to the high LiPs adsorption abilities associated with metal sulfides, and its high electrical conductivity, which would facilitate electronic transport and consequently promote the conversion of soluble LiPs into solid Li_2S_2/Li_2S. Nevertheless, $Fe_{1-x}S$ pyrrhotite has seldom been investigated as electrocatalyst in sulfur cathode for LSBs.[41,42] Porous carbon spheres as nanoreactors are currently gaining popularity in energy applications.[43] A nanoreactor is a standalone nanosized confined space that has been engineered with high surface area and pore volume, high number of active sites for a particular reaction and reduced mass transfer limitations for free transport of reactants and products. Therefore, combining the advantages of porous carbon spheres with highly dispersed $Fe_{1-x}S$ nanoparticles as electroactive sites is an attractive concept as nanoreactors for high-performance LSBs cathodes.

In this work, we adapt the Stöber protocol reported by Liu et al.[44] for the preparation of monodispersed resorcinol-formaldehyde (RF) resins and alter it to develop a simple one-step complexation modified Stöber (CMS) method to synthesize $Fe_{1-x}S$ electrocatalysts in N-doped porous carbon spheres ($Fe_{1-x}S$-NC) as nanoreactors having low mass density (due to high porosity) and high dispersion of $Fe_{1-x}S$ nanoparticles with low Fe content (0.96 wt%). For the first time, resorcinol sulfide is designed and selected as precursor for the synthesis of the molecular-level designed catalyst with uniformly distributed S in the framework. Such design 1) allows for homogeneous distribution of metal inside the polymer, 2) efficiently prevents the precipitation of metal hydroxide upon addition of ammonia during the polymerization reaction, 3) significantly creates close contact of Fe with S by chemical complexation to facilitate the formation of well dispersed $Fe_{1-x}S$ nanoparticles embedded within the carbon spheres upon carbonization, and furthermore 4) generates large mesoporous cavities in situ during high temperature carbonization resulting in low density, highly porous carbon spheres. The resultant $Fe_{1-x}S$-NC act as efficient nanoreactors with high loading of sulfur within conductive and porous carbon supports, amply decorated and highly accessible $Fe_{1-x}S$ nanosized electrocatalysts for LiPs adsorption and redox reaction. The excellent LiPs adsorption properties of the $Fe_{1-x}S$ nanoparticles in $Fe_{1-x}S$-NC is predicted by first principles calculations, and then confirmed experimentally. Thorough testing is carried out to establish the excellent electrocatalytic properties of $Fe_{1-x}S$ nanoparticles in $Fe_{1-x}S$-NC. It is shown that $Fe_{1-x}S$-NC has excellent performance as cathodic host for LSBs, exhibiting a high initial capacity of 1070 mAh g^{-1} that did not fade after 200 cycles at a rate of 0.5 C.

2. Results and Discussion

In this work, the metal precursor is directly added into the mixture during the polymer resin synthesis and resorcinol sulfide (RS) is used as a source of C and S. The sulfur in RS acts as a ligand to strongly bind with the metal cation via complexation. **Figure 1**a outlines the synthetic pathway for $Fe_{1-x}S$-NC nanospheres. Upon mixing of Fe^{3+} with an ethanol/water solution containing RS, a pink solution is obtained, proving the formation of an [Fe^{3+}–RS] complex. Then, aqueous NH_3 is added, turning the solution dark brown due to further formation of an [$Fe^{3+}NH_4^+$–RS] complex. As formaldehyde is added to induce polymerization, a milky brown precipitate of [$Fe^{3+}NH_4^+$–RS]–F resin with homogeneously distributed Fe^{3+} is gradually formed. When the experiment is carried out without addition of Fe^{3+}, a white precipitate is obtained (Figure S1, Supporting

© 2020 The Authors. Published by WILEY-VCH Verlag GmbH & Co. KGaA, Weinheim

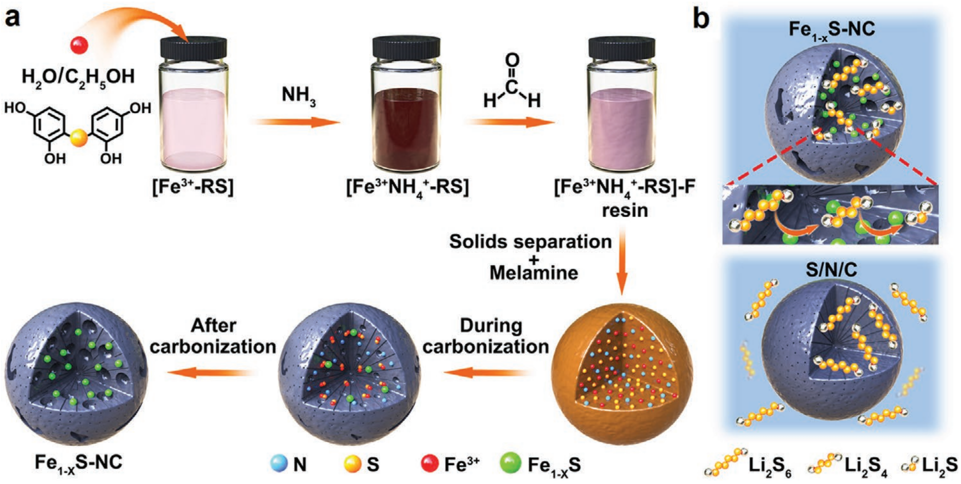

Figure 1. a) Steps involved in the synthesis of $Fe_{1-x}S$-NC spheres. b) Schematic illustration of hierarchical porous $Fe_{1-x}S$-NC acting as nanoreactor for the reduction of LiPs to Li_2S on nanosized $Fe_{1-x}S$ electrocatalysts while shuttling effect of LiPs occurs with S/N/C.

Information). The final brownish color of the precipitate in Figure 1a confirms that Fe^{3+} is indeed homogeneously distributed in the [$Fe^{3+}NH_4^+$–RS]–F resin by complexation. The brown resin is then thoroughly mixed with melamine (as a source of N) and finally carbonized in a 5% H_2/Ar mixture at 900 °C. Large mesoporous cavities and well dispersed $Fe_{1-x}S$ nanoparticles are gradually formed in situ within the carbon spheres during the carbonization process, resulting in the hierarchically porous $Fe_{1-x}S$-NC nanospheres. Meanwhile, the N species from melamine could control the dispersion of $Fe_{1-x}S$ by acting as anchorage points for Fe. A control sample of S and N doped carbon (S/N/C, prepared in a similar way except for the addition of the Fe^{3+}) was also prepared for comparison.

The adsorption and electrocatalytic properties of the $Fe_{1-x}S$ nanoparticles in the hierarchical porous $Fe_{1-x}S$-NC nanospheres is depicted in Figure 1b. $Fe_{1-x}S$ nanoparticles could effectively alleviate LiPs dissolution into the electrolyte due to the strong polar-polar interactions between $Fe_{1-x}S$ electrocatalyst and LiPs. Furthermore, $Fe_{1-x}S$ electrocatalyst could catalytically reduce soluble LiPs to Li_2S, leading to high S utilization and high LSB performance due to the diminution of the shuttle effect. On the other hand, S/N/C could neither provide strong interactions with the LiPs nor electrocatalytic activity, leading to the shuttling effect of LiPs (depicted in Figure 1b as the dissolution of LiPs into the electrolyte for S/N/C) and hence low LSB performance.

Transmission electron microscopy (TEM) images of $Fe_{1-x}S$-NC show the spheres of ≈250–300 nm in diameter in **Figure 2**a. Well dispersed nanoparticles of ≈20 nm size can be seen in the carbon spheres. Interestingly, obvious large mesoporous cavities could also be observed on/in the carbon spheres. The high magnification TEM image (Figure S2, Supporting Information) and high-angle annular dark-field (HAADF) image of $Fe_{1-x}S$-NC clearly show the Fe derived nanoparticles as well as the voids (Figure 2b1), and energy-dispersive X-ray spectroscopy (EDS) elemental mapping confirms the presence of C, N, O, Fe, and S (Figure 2b2–6). From the element mapping, it can be seen that C, N, and O are evenly distributed within the nanospheres. It is noted that Fe and S mapping coincide with the ≈20 nm sized nanoparticles, suggestive of the formation of Fe–S type nanoparticles. Scanning electron microscopy (SEM) image (Figure S3, Supporting Information) shows smooth particles with occasional cracks and cavities on the surfaces. Furthermore, the Fe–S-derived nanoparticles rarely appear on the sphere surfaces (one occurrence is pointed out by a yellow arrow in Figure S3 in the Supporting Information), from which we surmise that the nanoparticles are mostly embedded within the carbon spheres. The side-by-side scanning transmission electron microscopy (STEM; Figure 2c) and SEM images (Figure 2d) verify the presence of the cavities either on the spheres' surfaces or mostly as empty spaces inside the carbon spheres. High-resolution TEM (HRTEM) image (Figure 2e) of one nanoparticle discloses the lattice fringe *d*-spacings of 0.19 and 0.23 nm, corresponding to the (220) and (208) planes of hexagonal pyrrhotite $Fe_{1-x}S$, respectively. The mesoporous cavities observed in $Fe_{1-x}S$-NC are indeed not present in the control sample without Fe addition (S/N/C) which looks much denser than $Fe_{1-x}S$-NC (Figure S4a, Supporting Information). The presence of highly dispersed Fe may have catalytically induced the formation of cavities in $Fe_{1-x}S$-NC. It has been reported that the presence of Fe in graphite could greatly enhance the catalytic oxidation of carbon in CO_2–CO gas mixture at high temperature.[45] We therefore hypothesize that during the carbonization process of $Fe_{1-x}S$-NC, the CO_2 formed from pyrolysis gets adsorbed on the surface of the carbon while well dispersed Fe within the structure further reacts with structural carbon and the adsorbed CO_2 to give off CO gas. The enhanced oxidation of the structural carbon results in the mesoporous void spaces, as seen on the TEM, HAADF, and STEM images (Figure 2a,b 1,c), respectively. Furthermore, the use of a strongly reducing 5% H_2/Ar mixture as carbonization atmosphere helps to maintain the integrity of Fe during the catalytic oxidation reaction.

X-ray diffraction (XRD) patterns from Figure 2f show typical carbon peaks at ≈23° and 43° for both S/N/C and $Fe_{1-x}S$-NC. However, $Fe_{1-x}S$-NC has additional minor peaks at 30°, 33.9°, 43.8°, and 53.2° which are assigned to the (200), (204), (208), and (220) planes of hexagonal pyrrhotite $Fe_{1-x}S$, respectively

© 2020 The Authors. Published by WILEY-VCH Verlag GmbH & Co. KGaA, Weinheim

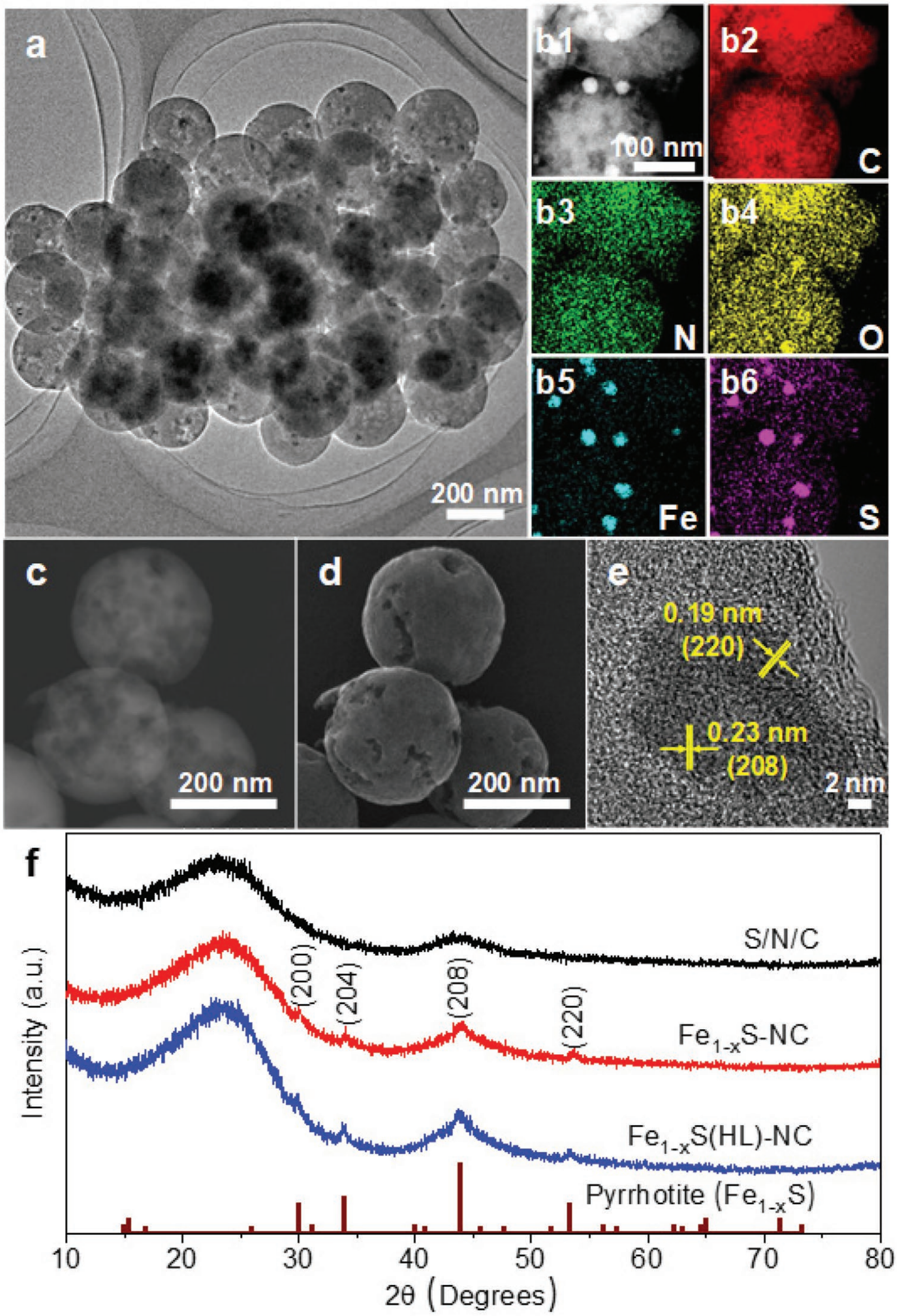

Figure 2. a) TEM image of $Fe_{1-x}S$-NC. b1) HAADF and b2–b6) elemental mapping of $Fe_{1-x}S$-NC. c) STEM image of $Fe_{1-x}S$-NC. d) SEM image of $Fe_{1-x}S$-NC. e) HRTEM image of $Fe_{1-x}S$ nanoparticle in $Fe_{1-x}S$-NC showing (220) and (208) lattice spacings and f) XRD patterns of S/N/C, $Fe_{1-x}S$-NC and $Fe_{1-x}S$(HL)-NC, with pyrrhotite ($Fe_{1-x}S$) as reference.

(JCPDS No. 22-1120). We synthesized a sample with higher loading of Fe ($Fe_{1-x}S$(HL)-NC), from which the XRD pattern in Figure 2f shows more obvious pyrrhotite peaks. The weight content of Fe in $Fe_{1-x}S$-NC was determined to be 0.96% via inductively coupled plasma atomic emission spectroscopy (ICP-AES). It is found that by increasing the Fe content in the carbon nanospheres, the size and dispersion of the $Fe_{1-x}S$ nanoparticles also change (Figures S4b,c, Supporting Information). The optimum dispersion of $Fe_{1-x}S$ nanoparticles is achieved at an Fe content of ≈1% (Figure S4b, Supporting Information). Beyond this amount, bigger nanoparticle aggregates are formed (Figure S4c, Supporting Information) and the carbon spheres

© 2020 The Authors. Published by WILEY-VCH Verlag GmbH & Co. KGaA, Weinheim

are much less porous, due to the reduced dispersion of Fe within the carbon support. N_2 adsorption–desorption isotherms for $Fe_{1-x}S$-NC and S/N/C are presented in Figure S5a (Supporting Information). Both materials show Type I isotherms, characteristic of microporous solids. The sharp inflexion at $P/P_0 > 0.9$ can be attributed to large macropores due to interparticle voids. Moreover, $Fe_{1-x}S$-NC N_2 isotherm shows clear hysteresis between adsorption and desorption branch while a slight hysteresis may be observed for S/N/C as well, which are due to the existence of mesopores. From the pore size distribution in Figure S5b (Supporting Information), it can be seen that both $Fe_{1-x}S$-NC and S/N/C contain micropores. However only $Fe_{1-x}S$-NC contains mesopores in the range of 8–20 nm, which are related to the interconnected cavities inside the spheres as seen in Figure 2a,b1,c. The textural parameters of the samples as determined from N_2 adsorption studies are presented in Table S1 (Supporting Information). Both $Fe_{1-x}S$-NC and S/N/C have large Brunauer–Emmett–Teller (BET) surface areas (S_{BET}) of 793 and 627 $m^2\ g^{-1}$ and total pore volumes (V_{total}) of 0.38 and 0.41 $cm^3\ g^{-1}$, respectively. Three types of pores exist in $Fe_{1-x}S$-NC, namely, micropores (0.199 $cm^3\ g^{-1}$), mesopores within the shell (0.001 $cm^3\ g^{-1}$), and the large mesoporous cavities within the nanospheres (0.213 $cm^3\ g^{-1}$). The hierarchical pore size distribution in $Fe_{1-x}S$-NC is ideal for Li–S batteries as this allows for efficient circulation of the electrolyte and unhindered distribution and diffusion of active species to and from the catalytic sites of the material. Furthermore, the large mesoporous cavities found in the nanospheres can accommodate reasonable amount of sulfur as well as buffer the volume expansion linked with Li insertion during the discharging process. The elemental electronic states and bonding configurations for $Fe_{1-x}S$-NC were investigated by X-ray photoelectron spectroscopy (XPS). The XPS survey spectrum (Figure S6, Supporting Information) confirms the presence of C, O, N, S, and Fe. The corresponding high-resolution XPS of Fe 2p and S 2p for $Fe_{1-x}S$-NC are presented in Figure S7a,b in the Supporting Information, respectively. The high-resolution XPS for Fe 2p shows the split spin-orbit components Fe $2p_{1/2}$ and Fe $2p_{3/2}$ as well as a broad peak at 717.6 eV attributed to Fe^{3+} $2p_{3/2}$ shake-up satellite.[46] The Fe $2p_{3/2}$ component is decomposed into 4 peaks at 709, 710.5, 712.1, and 714.1 eV, respectively. The binding energies (BEs) at 709, 710.5, and 712.1 eV can be attributed to the Fe^{3+} state, bound to S species,[47,48] while the high BE at 714.1 eV could be due to Fe^{3+} bound to longer chained polysulfides (S_n^{2-}) having larger electronegativity[49] or $Fe_2(SO_4)_3$.[48,50] The energy separation between the Fe^{3+} $2p_{3/2}$ shake-up satellite peak and the Fe $2p_{3/2}$ main peak (ΔE) indicates the type of ligand associated with Fe^{3+},[46] i.e., as the electronegativity of the ligand decreases, so does the ΔE. From Figure S7a (Supporting Information), the calculated $\Delta E = 7.1$ eV is much less than the values of 8.3–8.5 eV reported for Fe_2O_3.[46] These results imply that the ligand associated with Fe^{3+} in the nanoparticles of $Fe_{1-x}S$-NC is much less electronegative that O^{2-}, as is the case for S^{2-} and S_n^{2-}.[49] The S 2p peak has overlapping peak shape due to unresolved doublet (Figure S7b, Supporting Information). The S 2p component could be decomposed into three main peaks at 161.3, 163.8, and 167.8 eV, which were attributed to S^{2-}, S_n^{2-}, and possibly SO_4^{2-}, respectively.[47,48,51] The decomposed high-resolution XPS of C 1s, O 1s, and N 1s for $Fe_{1-x}S$-NC are presented in Figure S8a–c in the Supporting Information, respectively. It is noteworthy to point out that the signal for Fe–N_x species, typically at BE of around 399 eV[52,53] was not observed on the N 1s XPS for $Fe_{1-x}S$-NC (Figure S8c, Supporting Information). The N 1s, S 2p, and O 1s XPS spectra for S/N/C and $Fe_{1-x}S$-NC are compared and presented in Figure S9a–c in the Supporting Information, respectively, followed by discussions. From the characterization results discussed so far, it can be deduced that the Fe—S bond formed at molecular level from the complexation of RS with Fe^{3+} during the polymer synthesis strengthens and converts into $Fe_{1-x}S$ nanoparticles during the carbonization step. Meanwhile the N species, as it is well established,[54,55] act as anchoring points for the metal cations so as to prevent aggregation of the nanoparticles during thermal treatment. Indeed, without the addition of melamine, large nanoparticle aggregates are formed and preferentially migrate to the spheres' surfaces (Figure S10, Supporting Information). Finally, well dispersed Fe acts as a catalyst for the further cleavage/oxidation of the carbon skeleton (in the presence of CO, CO_2, and H_2) resulting in the large mesoporous voids in $Fe_{1-x}S$-NC. Raman spectroscopic studies (Figure S11, Supporting Information) reveal that both S/N/C and $Fe_{1-x}S$-NC possess a slightly graphitic character with similar I_G/I_D ratios of 1.08 and 1.1, respectively. The graphitic nature is attributed to the high pyrolysis temperature of 900 °C.

TGA studies in Figure S12 (Supporting Information) show that the amount of sulfur incorporated into S/N/C and $Fe_{1-x}S$-NC by melt/diffusion (denominated as S/N/C–S and $Fe_{1-x}S$-NC–S, respectively) are close or equal to the theoretical 75% loading determined from the cathode preparation protocol (see the Supporting Information). From the V_{total} values of the samples and the density of sulfur (2.07 g cm^{-3}), it can be calculated that most of the sulfur penetrates the samples' pores. The remaining sulfur probably covers the outer surface of the nanospheres following the melt-diffusion process. The temperatures at which all the sulfur vaporize from S/N/C–S and $Fe_{1-x}S$-NC–S are 450 and 400 °C, respectively, which are higher compared to 375 °C for pure elemental sulfur. The higher temperatures are due to the strong physical encapsulation of the sulfur inside the carbon micropores.[56] Furthermore the higher fraction of large mesopores in $Fe_{1-x}S$-NC–S reduced the degree of physical interaction of sulfur with the support which consequently reduced its vaporization temperature relative to S/N/C–S. XRD studies in Figure S13 (Supporting Information) highlight the interaction of sulfur with $Fe_{1-x}S$-NC–S. The lower peak intensities of sulfur in $Fe_{1-x}S$-NC–S compared to pure sulfur are attributed to the shielding effect of the carbon structure, manifesting that sulfur is successfully incorporated into the carbon spheres.

To evaluate the adsorption behavior of the LiPs with $Fe_{1-x}S$-NC, the static adsorption tests of LiPs was conducted by adding the same amount (1 mg) of $Fe_{1-x}S$-NC or S/N/C into 3 mL Li_2S_4 solution. Visually, the $Fe_{1-x}S$-NC shows high adsorption of the LiPs (**Figure 3**a) compared to S/N/C, which is consistent with the UV–vis spectra results showing a reduction in the absorbance peak at 417 nm for $Fe_{1-x}S$-NC (Figure 3b). The different adsorptions suggest more adsorbing sites on $Fe_{1-x}S$-NC. In addition, XPS analysis was carried out to investigate the chemical interaction between $Fe_{1-x}S$ and LiPs. The

© 2020 The Authors. Published by WILEY-VCH Verlag GmbH & Co. KGaA, Weinheim

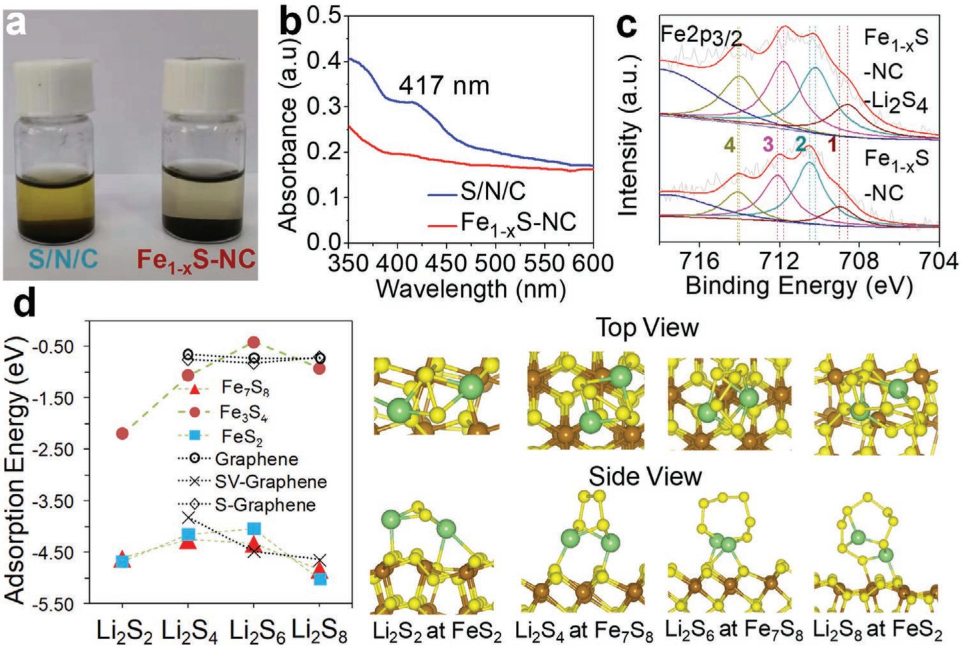

Figure 3. a) Variation in Li_2S_4 color upon adsorption by S/N/C and $Fe_{1-x}S$-NC, respectively. b) UV–vis spectra of Li_2S_4 upon adsorption by $Fe_{1-x}S$-NC and S/N/C, respectively. c) Fe 2p high-resolution XPS spectra for $Fe_{1-x}S$-NC before and after adsorption of Li_2S_4. d) Calculated adsorption energy of Li_2S_2, Li_2S_4, Li_2S_6, and Li_2S_8 on $Fe_{1-x}S$ surfaces together with previously published literature values on graphene,[57] graphene with single vacancy (SV),[57] and S-doped graphene.[57] For the larger molecules, it would be reasonable to expect a number of metastable adsorption configurations. Direct consideration is beyond the scope of this study.[57] The inserted schematics in d shows the strongest adsorption energy configurations, with yellow spheres for sulfur, brown for iron, and green for lithium.

Fe $2p_{3/2}$ XPS decompositions of $Fe_{1-x}S$-NC is compared with that of $Fe_{1-x}S$-NC after Li_2S_4 adsorption ($Fe_{1-x}S$-NC–Li_2S_4) in Figure 3c. For peaks 1, 2, and 3 which correspond to Fe^{3+}–S species, a clear shift to lower binding energies is observed on $Fe_{1-x}S$-NC–Li_2S_4 (change in binding energy between –0.3 and –0.4 eV). This confirms chemical binding of Li_2S_4 species to the $Fe_{1-x}S$ in the carbon spheres. Interestingly, for peak 4 corresponding to either $Fe_2(SO_4)_3$ or Fe^{3+} species bound to higher chained polysulfides, the shift in binding energy is negligible (–0.1 eV). It is suggested that $Fe_2(SO_4)_3$ is most probably the dominant species from spectrum 4 and does not interact with Li_2S_4 species. Therefore, XPS analysis of Fe $2p_{3/2}$ for $Fe_{1-x}S$-NC compared to $Fe_{1-x}S$-NC–Li_2S_4 confirms the strong interaction between $Fe_{1-x}S$ nanoparticles in the carbon spheres with Li_2S_4 species in the electrolyte.

To assess the stronger adsorption of LiPs (Li_2S_2, Li_2S_4, Li_2S_6, and Li_2S_8) on $Fe_{1-x}S$-NC, as compared to S/N/C, density functional theory (DFT) simulations of LiPs on $Fe_{1-x}S$ are conducted using the Vienna Ab Initio Simulation Package (VASP).[58–61] To study the LiPs adsorption energies on pyrrhotite ($Fe_{1-x}S$), surface models of Fe_7S_8, FeS_2, and Fe_3S_4 are employed in accordance with previous literatures.[62–67] For the surface calculations, we study the (001) surfaces, which have previously been shown to be the most stable surface termination for these materials.[67] These surface models have previously been used to study the sodium storage in $Fe_{1-x}S/MoS_2$ composites,[62] as a monolayer for oxygen evolution reaction,[63] and for oxygen incorporation.[65] The adsorption energies of LiPs on different carbon sulfur nitrogen structures have been well studied in the literature and are hence only discussed briefly here.[57,66,68–74] The adsorption of LiPs has been shown to be improved by the addition of vacancy defects on graphene, and by heteroatom doping of graphene sheets. The LiPs adsorption energy on pristine graphene has been reported, ranging from –0.17 to 0.73 eV for LiPs.[57,66,68,75] By the inclusion of a single vacancy (SV) defect in graphene, the adsorption strength was seen to increase,[57,66] whereas sulfur and nitrogen doping of the graphene sheet was not found to enhance the LiPs adsorption markedly.[57] Similarly, the inclusion of Stone–Wales (SW) defects on the graphene sheet did not increase the LiPs adsorption energy markedly.[57] Fe- and FeN_4-doping of graphene was also shown to strengthen the LiPs adsorption, indicating that LiPs binding to iron-containing substrate could enhance the adsorption performance.[73] A collection of LiPs adsorption energies on different substrates is included in Table S2 in the Supporting Information.

The adsorption energy (E_{ads}) of LiPs on the pyrrhotite surfaces were calculated according to Equation (1)

$$E_{ads} = E_{Li_2S_x \text{ at } Fe_{1-x}S} - E_{Li_2S_x} - E_{Fe_{1-x}S} \tag{1}$$

where $E_{Li_2S_x \text{ at } Fe_{1-x}S}$ is the total energy of LiPs adsorbed on the surface, $E_{Fe_{1-x}S}$ is the total energy of the surface, and $E_{Li_2S_x}$ is the total energy of one LiPs molecule isolated in a 20 Å × 20 Å × 20 Å vacuum box.[66,70,72] The adsorption energies of LiPs on pyrrhotite surfaces (Fe_7S_8, Fe_3S_4, and FeS_2) are presented in Figure 3d and in Table S2 in the Supporting Information. It is clear that LiPs adsorption on all the herein investigated $Fe_{1-x}S$ surfaces is energetically favorable, with negative adsorption energies. The Fe_3S_4 surface is less energetically favorable for LiPs adsorption, with adsorption energies in the range of the

© 2020 The Authors. Published by WILEY-VCH Verlag GmbH & Co. KGaA, Weinheim

reported values for graphene and other materials. The adsorption of LiPs on Fe_7S_8 and FeS_2 surfaces are much stronger and show very similar adsorption strengths, with adsorption energies comparable or stronger to that reported for SV graphene.[57,66] The structural configurations (top and side views) of the most favorable adsorption sites for Li_2S_2, Li_2S_4, Li_2S_6, and Li_2S_8, respectively, are inset in Figure 3d (other energetically favorable configurations are summarized in Figures S14–S17 (Supporting Information) for Fe_7S_8 and Figures S18–S21 (Supporting Information) for FeS_2). All LiPs show most stable adsorption structures with Li oriented closest to the surface, with the S_x chain oriented away from the surface, except for Li_2S_8 where one S adsorbs over a Fe-site. Both Li_2S_2 and Li_2S_8 adsorption on FeS_2 are the most strongly bonded with adsorption energies of –4.68 and –5.01 eV, respectively. For the intermediate LiPs, Li_2S_4, and Li_2S_6, the adsorption on the Fe_7S_8 is more energetically favorable, with similarly strong adsorption energies of –4.25 and –4.33 eV, respectively. In brief, the adsorption of LiPs is highly improved on the $Fe_{1-x}S$ surfaces, as compared to carbon surfaces.

To demonstrate the electrocatalytic properties of $Fe_{1-x}S$-NC, the Li_2S precipitation experiments on the surface of $Fe_{1-x}S$-NC and S/N/C were designed. The cell was galvanostatically discharged to 2.06 V and then kept at 2.05 V until the current was lower than 10^{-5} A. The responsiveness of Li_2S nucleation is earlier on $Fe_{1-x}S$-NC than on S/N/C. Moreover, the capacities of Li_2S precipitation on $Fe_{1-x}S$-NC (83.6 mAh g^{-1}) are much higher than on S/N/C (26.9 mAh g^{-1}) (**Figure** 4a,b). These results clearly show that $Fe_{1-x}S$-NC promotes the fast conversion of LiPs to Li_2S. The sluggish kinetics of the oxidation of solid Li_2S during the charge process is the main reason for oxidation overpotential in a working LSB.[75] To prove the positivity of promoting Li_2S dissolution, the kinetic evaluation of Li_2S dissolution was performed using a potentiostatic charge method after full discharge into Li_2S. An obvious oxidative peak of Li_2S dissolution at 553 s is detected on $Fe_{1-x}S$-NC (Figure 4c). In contrast, smaller and delayed (875 s) current signal is observed for S/N/C, suggesting the excellent electrocatalytic properties of $Fe_{1-x}S$-NC in promoting Li_2S dissolution. The catalytic effect is further demonstrated by the cyclic voltammetry (CV) results of Li_2S_6–Li_2S_6 symmetric cells (Figure 4d). $Fe_{1-x}S$-NC exhibits a higher current density than that of S/N/C, implying the significantly enhanced redox kinetics with liquid-phase polysulfides. A comparison of the CV curves for $Fe_{1-x}S$-NC and S/N/C is presented and explained (in terms of polysulfides redox kinetics) in Figure S22 (Supporting Information). In addition, the forward scan (Figure S23a, Supporting Information) shows higher scanning current densities for $Fe_{1-x}S$-NC compared to S/N/C and a smaller Tafel slope of 279 mV $decade^{-1}$ for $Fe_{1-x}S$-NC electrode as opposed to 290 mV $decade^{-1}$ for S/N/C (Figure S23b, Supporting Information), confirming the enhanced reaction kinetics for LiPs redox reactions by $Fe_{1-x}S$-NC. All in all, these results further demonstrate that the kinetics of polysulfide redox reactions are effectively improved by $Fe_{1-x}S$ nanoparticles in $Fe_{1-x}S$-NC.

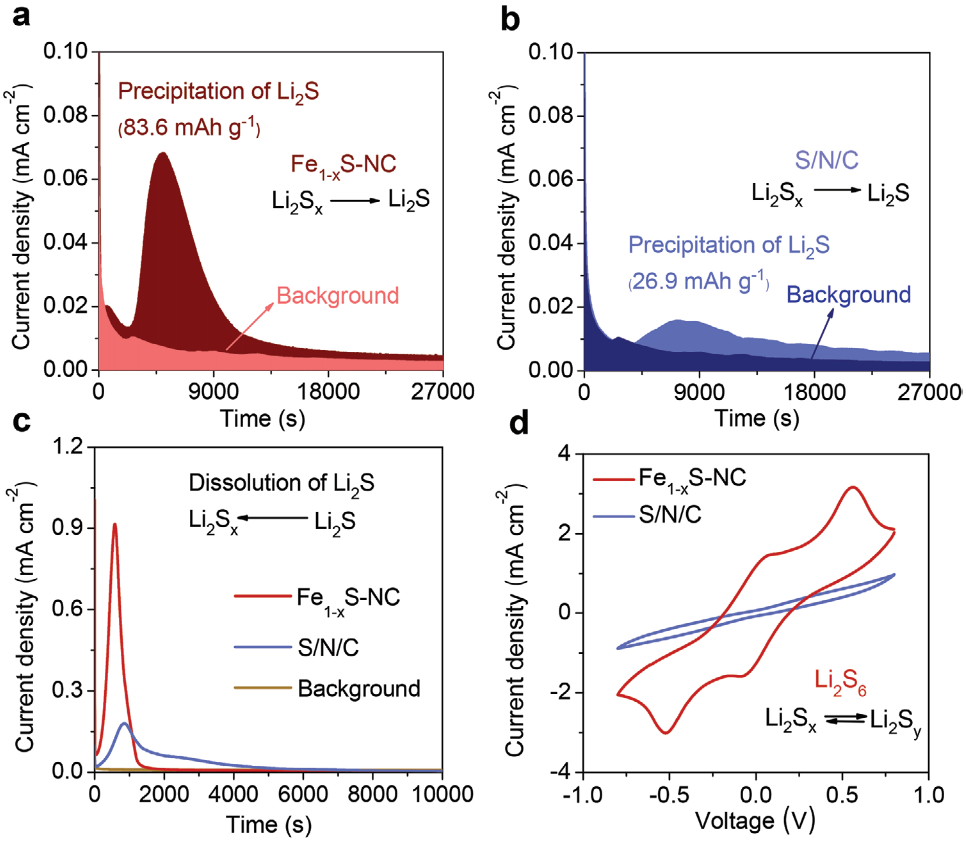

Figure 4. Potentiostatic discharge profiles of a Li_2S_8/tetraglyme solution on a) $Fe_{1-x}S$-NC and b) S/N/C at 2.05 V. c) Potentiostatic charge profile at 2.40 V for evaluating dissolution kinetics of Li_2S, and d) CV curves of Li_2S_6 symmetric cells using $Fe_{1-x}S$-NC and S/N/C electrodes at a scan rate of 5 mV s^{-1}.

© 2020 The Authors. Published by WILEY-VCH Verlag GmbH & Co. KGaA, Weinheim

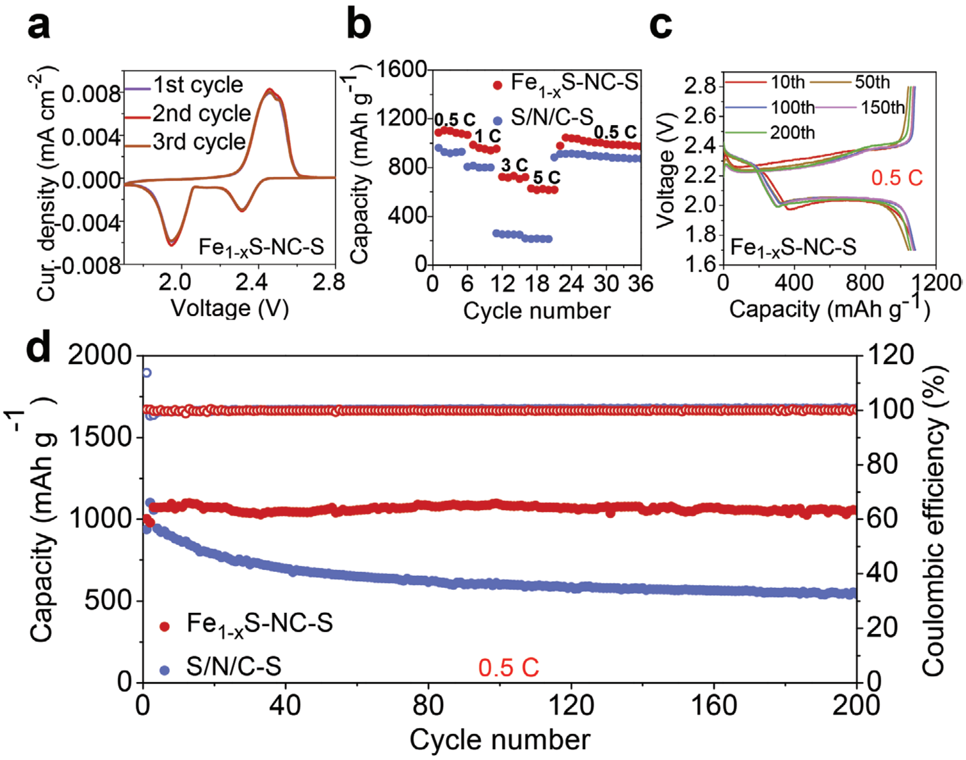

Figure 5. a) CV curves of the $Fe_{1-x}S$-NC–S for LSBs in a potential window from 1.7 to 2.8 V. b) Rate capability of $Fe_{1-x}S$-NC–S and S/N/C–S for LSBs. c) Charge/discharge profiles of $Fe_{1-x}S$-NC–S for LSBs obtained at 0.5 C (1 C = 1675 mAh g^{-1}) and d) cycling stability of $Fe_{1-x}S$-NC–S and S/N/C–S LSB cells at 0.5 C over 200 cycles.

To reveal the role of the $Fe_{1-x}S$-NC on Li–S batteries, the electrochemical performances were measured with the $Fe_{1-x}S$-NC–S cathode (sulfur-loaded $Fe_{1-x}S$-NC).The initial three CV curves of $Fe_{1-x}S$-NC–S cathode, tested in the range of 1.7–2.8 V at 0.1 mV s^{-1}, show negligible current changes and potential shifts in these CV peaks (**Figure 5**a), indicating outstanding electrochemical stability. The $Fe_{1-x}S$-NC–S cathode presents much better rate capability compared to the S/N/C–S cathode (Figure 5b), especially at high current density due to the enhanced electrocatalytic properties of $Fe_{1-x}S$ particles. Under different current rates of 0.5, 1, 3, and 5 C, the capacities of $Fe_{1-x}S$-NC–S electrode are 1106, 981, 730, and 628 mAh g^{-1}, respectively; while for S/N/C–S cathode, the corresponding capacities decrease to 956, 822, 252, and 222 mAh g^{-1}, respectively. The galvanostatic discharge-charge profiles were then performed at a constant current rate of 0.5 C (Figure 5c). The discharge curves consist of two reduction plateaus at 2.3 and 2.0 V, respectively, while the charge curves consist of one long oxidation plateau at 2.4 V. From the cycling stability at 0.5 C in Figure 5d, the $Fe_{1-x}S$-NC–S cathode exhibits a high initial capacity of 1070 mAh g^{-1} which maintains at 1064 mAh g^{-1} after 200 cycles, rendering an ultralow capacity fading rate of 0.003% per cycle, i.e., barely no change in capacity. This performance greatly outperforms other reported sulfide-based cathodes by one to two orders of magnitude, as presented in Table S3 (Supporting Information). In contrast, the S/N/C–S delivers much lower capacity of 940 mAh g^{-1} which maintains at 547 mAh g^{-1} after 200 cycles, corresponding to a high capacity fading rate of 0.2% per cycle. Please note that the high initial Coulombic efficiency for S/N/C–S in Figure 5d is probably related to the unstable solid electrolyte interface (SEI) at both the sulfur cathode and lithium anode. These results demonstrate that the incorporation of $Fe_{1-x}S$ nanoparticles into the carbon spheres efficiently mitigate the LiPs dissolution into the organic electrolyte. To illustrate the electrochemical kinetics of these two electrodes, electrochemical impedance spectroscopy (EIS) measurements were conducted (Figure S24, Supporting Information). The $Fe_{1-x}S$-NC–S electrode exhibits smaller charge-transfer resistance (19.2 Ω) than that of S/N/C–S electrode (29.1 Ω), indicative of greatly reduced internal resistance in $Fe_{1-x}S$-NC–S. The lower charge-transfer resistance implies a faster charge/mass transfer rate, which is beneficial for high rate capability. This is certainly attributed to the good dispersion of the conductive $Fe_{1-x}S$ nanoparticles within the carbon spheres as well as the presence of cavities and mesopores that allow for efficient migration of the LiPs. As shown in the charge/discharge curves (Figure S25a,b, Supporting Information), the plateau of $Fe_{1-x}S$-NC–S is flatter and more stable with a low polarization hysteresis of 172 mV at 0.5 C, while in the case of S/N/C–S cathode, a bigger voltage hysteresis of 268 mV is attained, suggestive of enhanced interfacial kinetics and Li^+/e^- transport due to the presence of $Fe_{1-x}S$ nanoparticles and hierarchical porosity of the catalyst. The long-term cycling stability was further studied at 1 C (Figure S26, Supporting Information). Remarkably, $Fe_{1-x}S$-NC–S electrode delivers a high capacity of 793 mAh g^{-1} after 200 cycles, corresponding to high capacity retention of 84%. In contrast, without $Fe_{1-x}S$, the electrode achieves much lower capacity of 565 mAh g^{-1}.

© 2020 The Authors. Published by WILEY-VCH Verlag GmbH & Co. KGaA, Weinheim

High sulfur loading (8.14 mg cm^{-2}) of the $Fe_{1-x}S$-NC–S cathode was also tested (Figure S27, Supporting Information). Impressively, a high areal capacity of 7.4 mAh cm^{-2} is achieved, and 5.10 mAh cm^{-2} is retained after 60 cycles, demonstrating the potential application value of our hierarchically porous $Fe_{1-x}S$-NC spheres as nanoreactors for high-performance cathodes in LSBs. Overall, $Fe_{1-x}S$-NC act as individual nanoreactors with hierarchical pores acting as channels for efficient electrolyte distribution and diffusion of species to and from active sites. The active sites consist of highly dispersed, accessible and electrically conductive $Fe_{1-x}S$ nanoparticles that are excellent at adsorbing and reducing LiPs. Finally, the presence of large mesoporous cavities in the carbon spheres ensures high sulfur loading and contacting with the electrically conductive carbon, as well as modulating the large volume variations associated with charge/discharge cycles. Combined, all these properties make $Fe_{1-x}S$-NC an excellent cathodic nanoreactor for LSBs.

3. Conclusion

A general one-step method is successfully employed for the molecular design and synthesis of dispersed $Fe_{1-x}S$ nanoparticles embedded in N doped carbon spheres ($Fe_{1-x}S$-NC). The high electrocatalytic activity of $Fe_{1-x}S$ nanoparticles coupled with their high electronic conductivity and accessibility allow for efficient adsorption and conversion of LiPs to Li_2S. The electrocatalysts are well dispersed in the hierarchically porous carbon spheres with large mesoporous cavities, which can accommodate high sulfur loading, modulate volume variations during charge/discharge cycles and enhance mass transfer of electrolyte to active sites. As a result, high-performance cathode with exceptional stability (no capacity fading at 0.5 C after 200 cycles), high rate capability and excellent cycling performance at high sulfur loading of 8.14 mg cm^{-2}, are achieved for LSBs. This work demonstrates the potential applicability of well dispersed metal sulfides at low metal loading inside highly porous carbon spheres as high-performance nanoreactors for LSBs. The results can also open opportunities for construction of more complex architectures such as hollow structures, yolk–shell or multishell particles doped with metal sulfides via molecular-level design to improve the performance of LSBs in terms of long-term cycling stability and high sulfur loading. Molecular level design could also be an attractive method for the synthesis of highly dispersed metal nitrides, oxides, phosphides, or halides inside a carbon support by the suitable choice of a precursor and synthesis methods.

Supporting Information

Supporting Information is available from the Wiley Online Library or from the author.

Acknowledgements

Y.B. and H.D.S. contributed equally to this work. The authors would like to thank A/Prof. Na Ta and Prof. Hongyang Liu for the assistance of TEM characterization. This work was supported financially by the Dalian National Laboratory for Clean Energy (DNL), CAS, DNL Cooperation Fund, CAS (DNL180402, DNL180310, DNL180308, DNL201912, and DNL201915), the Engineering and Physical Sciences Research Council for funding (EP/R021554/1), National Key R&D Program of China (Grant 2016YBF0100100), National Natural Science Foundation of China (Grant Nos. 51872283 and 21805273), Natural Science Foundation of Liaoning Province, Joint Research Fund Liaoning-Shenyang National Laboratory for Materials Science (Grant 20180510038), Liaoning Revitalization Talents Program (Grant Nos. XLYC1807077 and XLYC1807153), DICP (DICP ZZBS201708 and DICP ZZBS201802), and DICP&QIBEBT (Grant Nos. DICP and QIBEBT UN201702). E.O. would like to acknowledge the use of Athena at HPC Midlands+, which was funded by the EPSRC under grant EP/P020232/1, and the Eureka HPC cluster at the University of Surrey. The authors are grateful to the UK Materials and Molecular Modelling Hub for computational resources, which is partially funded by EPSRC (EP/P020194/1).

Conflict of Interest

The authors declare no conflict of interest.

Keywords

electrocatalytic effects, lithium–sulfur batteries, metal sulfides, porous carbon spheres, pyrrhotite

Received: February 19, 2020
Revised: March 11, 2020
Published online: April 16, 2020

---

[1] A. Manthiram, S. H. Chung, C. Zu, *Adv. Mater.* **2015**, *27*, 1980.
[2] N. Jayaprakash, J. Shen, S. S. Moganty, A. Corona, L. A. Archer, *Angew. Chem., Int. Ed.* **2011**, *50*, 5904.
[3] J. Kim, D. J. Lee, H. G. Jung, Y. K. Sun, J. Hassoun, B. Scrosati, *Adv. Funct. Mater.* **2013**, *23*, 1076.
[4] Z. W. Seh, Y. Sun, Q. Zhang, Y. Cui, *Chem. Soc. Rev.* **2016**, *45*, 5605.
[5] G. Zhou, S. Zhao, T. Wang, S. Z. Yang, B. Johannessen, H. Chen, C. Liu, Y. Ye, Y. Wu, Y. Peng, C. Liu, S. P. Jiang, Q. Zhang, Y. Cui, *Nano Lett.* **2020**, *20*, 1252.
[6] C. Ye, D. Chao, J. Shan, H. Li, K. Davey, S. Z. Qiao, *Matter* **2020**, *2*, 323.
[7] S. H. Chung, C. H. Chang, A. Manthiram, *Adv. Funct. Mater.* **2018**, *28*, 1801188.
[8] Y. X. Yin, S. Xin, Y. G. Guo, L. J. Wan, *Angew. Chem., Int. Ed.* **2013**, *52*, 13186.
[9] J. Guo, Y. Xu, C. Wang, *Nano Lett.* **2011**, *11*, 4288.
[10] Z. Li, J. Zhang, B. Guan, D. Wang, L.-M. Liu, X. W. D. Lou, *Nat. Commun.* **2016**, *7*, 13065.
[11] H. J. Peng, T. Z. Hou, Q. Zhang, J. Q. Huang, X. B. Cheng, M. Q. Guo, Z. Yuan, L. Y. He, F. Wei, *Adv. Mater. Interfaces* **2014**, *1*, 1400227.
[12] J. Zhang, C. P. Yang, Y. X. Yin, L. J. Wan, Y. G. Guo, *Adv. Mater.* **2016**, *28*, 9539.
[13] L. Luo, S. H. Chung, H. Yaghoobnejad Asl, A. Manthiram, *Adv. Mater.* **2018**, *30*, 1804149.
[14] Z.-L. Xu, S. Lin, N. Onofrio, L. Zhou, F. Shi, W. Lu, K. Kang, Q. Zhang, S. P. Lau, *Nat. Commun.* **2018**, *9*, 4164.
[15] X. Liu, J. Q. Huang, Q. Zhang, L. Mai, *Adv. Mater.* **2017**, *29*, 1601759.
[16] S. J. Kim, K. Kim, J. Park, Y. E. Sung, *ChemCatChem* **2019**, *11*, 2373.
[17] X. Liang, C. Y. Kwok, F. Lodi-Marzano, Q. Pang, M. Cuisinier, H. Huang, C. J. Hart, D. Houtarde, K. Kaup, H. Sommer, *Adv. Energy Mater.* **2016**, *6*, 1501636.

© 2020 The Authors. Published by WILEY-VCH Verlag GmbH & Co. KGaA, Weinheim

[18] X. Chen, H.-J. Peng, R. Zhang, T.-Z. Hou, J.-Q. Huang, B. Li, Q. Zhang, *ACS Energy Lett.* **2017**, *2*, 795.
[19] Z. W. Seh, J. H. Yu, W. Li, P.-C. Hsu, H. Wang, Y. Sun, H. Yao, Q. Zhang, Y. Cui, *Nat. Commun.* **2014**, *5*, 5017.
[20] Z. Sun, J. Zhang, L. Yin, G. Hu, R. Fang, H.-M. Cheng, F. Li, *Nat. Commun.* **2017**, *8*, 14627.
[21] D. H Liu, C. Zhang, G. M. Zhou, W. Lv, G. W. Ling, L. J. Zhi, Q. H. Yang, *Adv. Sci.* **2018**, *5*, 1700270.
[22] J. Xu, W. Zhang, H. Fan, F. Cheng, D. Su, G. Wang, *Nano Energy* **2018**, *51*, 73.
[23] A. Manthiram, Y. Fu, S.-H. Chung, C. Zu, Y.-S. Su, *Chem. Rev.* **2014**, *114*, 11751.
[24] Q. Sun, B. He, X.-Q. Zhang, A.-H. Lu, *ACS Nano* **2015**, *9*, 8504.
[25] W. Zhou, Y. Yu, H. Chen, F. J. DiSalvo, H. c. D. Abruña, *J. Am. Chem. Soc.* **2013**, *135*, 16736.
[26] Z. W. Seh, W. Li, J. J. Cha, G. Zheng, Y. Yang, M. T. McDowell, P.-C. Hsu, Y. Cui, *Nat. Commun.* **2013**, *4*, 1331.
[27] S. Chen, X. Huang, B. Sun, J. Zhang, H. Liu, G. Wang, *J. Mater. Chem. A* **2014**, *2*, 16199.
[28] J. Wang, J. Wan, N. Yang, Q. Li, D. Wang, *Nat. Rev. Chem.* **2020**, *4*, 159.
[29] J. Liu, T. Yang, D. W. Wang, G. Q. Lu, D. Zhao, S. Z. Qiao, *Nat. Commun.* **2013**, *4*, 2798.
[30] T. Yang, Y. Zhong, J. Liang, M. M. Rahman, W. Lei, Y. Chen, M. J. Monteiro, Z. Shao, J. Liu, *Part. Part Syst. Charact.* **2017**, *34*, 1600281.
[31] Z. Yuan, H.-J. Peng, T.-Z. Hou, J.-Q. Huang, C.-M. Chen, D.-W. Wang, X.-B. Cheng, F. Wei, Q. Zhang, *Nano Lett.* **2016**, *16*, 519.
[32] T. Lei, W. Chen, J. Huang, C. Yan, H. Sun, C. Wang, W. Zhang, Y. Li, J. Xiong, *Adv. Energy Mater.* **2017**, *7*, 1601843.
[33] A. Douglas, R. Carter, L. Oakes, K. Share, A. P. Cohn, C. L. Pint, *ACS Nano* **2015**, *9*, 11156.
[34] G. Zhou, H. Tian, Y. Jin, X. Tao, B. Liu, R. Zhang, Z. W. Seh, D. Zhuo, Y. Liu, J. Sun, J. Zhao, C. Zu, D. S. Wu, Q. Zhang, Y. Cui, *Proc. Natl. Acad. Sci. USA* **2017**, *114*, 840.
[35] X. Huang, J. Tang, B. Luo, R. Knibbe, T. Lin, H. Hu, M. Rana, Y. Hu, X. Zhu, Q. Gu, *Adv. Energy Mater.* **2019**, *9*, 1901872.
[36] T. Chen, Z. Zhang, B. Cheng, R. Chen, Y. Hu, L. Ma, G. Zhu, J. Liu, Z. Jin, *J. Am. Chem. Soc.* **2017**, *139*, 12710.
[37] Y. Song, H. Wang, W. Yu, J. Wang, G. Liu, D. Li, T. Wang, Y. Yang, X. Dong, Q. Ma, *J. Power Sources* **2018**, *405*, 51.
[38] W. Li, J. Qian, T. Zhao, Y. Ye, Y. Xing, Y. Huang, L. Wei, N. Zhang, N. Chen, L. Li, *Adv. Sci.* **2019**, *6*, 1802362.
[39] C. I. Pearce, R. A. Pattrick, D. J. Vaughan, *Rev. Mineral. Geochem.* **2006**, *61*, 127.
[40] S. S. Zhang, D. T. Tran, *J. Mater. Chem. A* **2016**, *4*, 4371.
[41] J. H. Ahn, G. K. Veerasubramani, S.-M. Lee, T.-S. You, D.-W. Kim, *J. Electrochem. Soc.* **2019**, *166*, A5201.
[42] K. Zhang, F. Chen, H. Pan, L. Wang, D. Wang, Y. Jiang, L. Wang, Y. Qian, *Inorg. Chem. Front.* **2019**, *6*, 477.
[43] H. Tian, J. Liang, J. Liu, *Adv. Mater.* **2019**, *31*, 1903886.
[44] J. Liu, S. Z. Qiao, H. Liu, J. Chen, A. Orpe, D. Zhao, G. Q. Lu, *Angew. Chem., Int. Ed.* **2011**, *50*, 5947.
[45] E. Turkdogan, J. Vinters, *Carbon* **1972**, *10*, 97.
[46] A. Grosvenor, B. Kobe, M. Biesinger, N. McIntyre, *Surf. Interface Anal.* **2004**, *36*, 1564.
[47] J. E. Thomas, W. M. Skinner, R. S. Smart, *Geochim. Cosmochim. Acta* **2003**, *67*, 831.
[48] A. Matamoros-Veloza, O. Cespedes, B. R. Johnson, T. M. Stawski, U. Terranova, N. H. de Leeuw, L. G. Benning, *Nat. Commun.* **2018**, *9*, 3125.
[49] J. B. Martin, A. W. Davidson, *Trans. Kans. Acad. Sci.* **1940**, *43*, 227.
[50] D. Brion, *Appl. Surf. Sci.* **1980**, *5*, 133.
[51] R. S. C. Smart, W. M. Skinner, A. R. Gerson, *Surf. Interface Anal.* **1999**, *28*, 101.
[52] H. Zhang, S. Hwang, M. Wang, Z. Feng, S. Karakalos, L. Luo, Z. Qiao, X. Xie, C. Wang, D. Su, *J. Am. Chem. Soc.* **2017**, *139*, 14143.
[53] W.-J. Jiang, L. Gu, L. Li, Y. Zhang, X. Zhang, L.-J. Zhang, J.-Q. Wang, J.-S. Hu, Z. Wei, L.-J. Wan, *J. Am. Chem. Soc.* **2016**, *138*, 3570.
[54] H.-W. Liang, W. Wei, Z.-S. Wu, X. Feng, K. Müllen, *J. Am. Chem. Soc.* **2013**, *135*, 16002.
[55] W. Ju, A. Bagger, G.-P. Hao, A. S. Varela, I. Sinev, V. Bon, B. R. Cuenya, S. Kaskel, J. Rossmeisl, P. Strasser, *Nat. Commun.* **2017**, *8*, 944.
[56] C. Zhang, H. B. Wu, C. Yuan, Z. Guo, X. W. Lou, *Angew. Chem., Int. Ed.* **2012**, *51*, 9592.
[57] S. P. Jand, Y. Chen, P. Kaghazchi, *J. Power Sources* **2016**, *308*, 166.
[58] G. Kresse, J. Furthmüller, *Phys. Rev. B* **1996**, *54*, 11169.
[59] G. Kresse, J. Furthmüller, *Comp. Mater. Sci.* **1996**, *6*, 15.
[60] G. Kresse, J. Hafner, *Phys. Rev. B* **1993**, *47*, 558.
[61] G. Kresse, J. Hafner, *Phys. Rev. B* **1994**, *49*, 14251.
[62] S. Chen, S. Huang, J. Hu, S. Fan, Y. Shang, M. E. Pam, X. Li, Y. Wang, T. Xu, Y. Shi, *Nano–Micro Lett.* **2019**, *11*, 80.
[63] S. Chen, Z. Kang, X. Zhang, J. Xie, H. Wang, W. Shao, X. Zheng, W. Yan, B. Pan, Y. Xie, *ACS Cent. Sci.* **2017**, *3*, 1221.
[64] M. J. Schaible, H. P. Pinto, A. D. McKee, J. Leszczynski, T. M. Orlando, *J. Phys. Chem. C* **2019**, *123*, 26397.
[65] U. Terranova, C. Mitchell, M. Sankar, D. Morgan, N. H. de Leeuw, *J. Phys. Chem. C* **2018**, *122*, 12810.
[66] Z. Yi, F. Su, L. Huo, G. Cui, C. Zhang, P. Han, N. Dong, C. Chen, *Appl. Surf. Sci.* **2020**, *503*, 144446.
[67] C.-H. Zhao, J.-H. Chen, Y.-Q. Li, C. Ye, W.-Z. Li, *Trans. Nonferrous Met. Soc. China* **2016**, *26*, 519.
[68] Y. Cao, Y. Lin, J. Wu, X. Huang, Z. Pei, J. Zhou, G. Wang, *ChemSusChem* **2019**, *13*, 1392.
[69] W. He, X. He, M. Du, S. Bie, J. Liu, Y. Wang, M. Liu, Z. Zou, W. Yan, H. Zhao, *J. Phys. Chem. C* **2019**, *123*, 15924.
[70] H. Lin, D.-D. Yang, N. Lou, S.-G. Zhu, H.-Z. Li, *Ceram. Int.* **2019**, *45*, 1588.
[71] Y. Shao, Q. Wang, L. Hu, H. Pan, X. Shi, *Carbon* **2019**, *149*, 530.
[72] T.-T. Yu, P.-F. Gao, Y. Zhang, S.-L. Zhang, *Appl. Surf. Sci.* **2019**, *486*, 281.
[73] L. Zhang, P. Liang, X.-l. Man, D. Wang, J. Huang, H.-b. Shu, Z.-g. Liu, L. Wang, *J. Phys. Chem. Solids* **2019**, *126*, 280.
[74] Y. Zhang, S.-Y. Li, H. Huang, W.-T. Li, J.-B. Qiao, W.-X. Wang, L.-J. Yin, K.-K. Bai, W. Duan, L. He, *Phys. Rev. Lett.* **2016**, *117*, 166801.
[75] H. Yuan, H. J. Peng, B. Q. Li, J. Xie, L. Kong, M. Zhao, X. Chen, J. Q. Huang, Q. Zhang, *Adv. Energy Mater.* **2019**, *9*, 1802768.